

We are IntechOpen, the world's leading publisher of Open Access books Built by scientists, for scientists

6,900

Open access books available

186,000

International authors and editors

200M

Downloads

Our authors are among the

154

Countries delivered to

TOP 1%

most cited scientists

12.2%

Contributors from top 500 universities



WEB OF SCIENCE™

Selection of our books indexed in the Book Citation Index
in Web of Science™ Core Collection (BKCI)

Interested in publishing with us?
Contact book.department@intechopen.com

Numbers displayed above are based on latest data collected.
For more information visit www.intechopen.com



Oriented Lateral Growth and Defects in Polycrystalline-Silicon Thin Films on Glass Substrates

Kuninori Kitahara¹ and Akito Hara²

¹*Shimane University*

²*Tohoku Gakuin University*
Japan

1. Introduction

Silicon (Si) thin films on glass substrates have been extensively developed as a semiconductor material for electronic devices. This material is especially useful for large-area panel devices such as thin-film transistors (TFTs) on active-matrix flat panel displays. The most widely used Si films are hydrogenated amorphous Si (a-Si:H), which can be deposited at temperatures lower than the strain point of the substrate. However, improved electronic properties are required to achieve higher device performance. Using polycrystalline Si (poly-Si) films instead of a-Si:H films enhances carrier mobility by two or three orders of magnitude; thus, driver circuits can be incorporated into display panels, as shown in Fig. 1. The application of poly-Si will be extended to mobile displays with large pixel density, microprocessor-display combined panels, and thin-film solar cells.

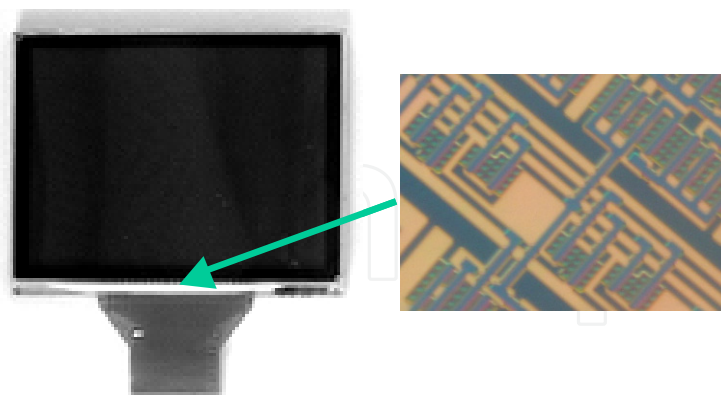


Fig. 1. Low-temperature poly-Si liquid crystal display (2 in. diagonal). Driver circuits are integrated at the periphery of the panel.

The poly-Si used for TFT must be ≤ 50 nm thick to ensure the desired device performance. Furthermore, the crystalline fraction should be almost 100%. Such thin films cannot be deposited directly on glass; they must be formed by recrystallization of a-Si precursor films. For this purpose, manufactures have employed solid-phase crystallization (SPC) and

excimer-laser crystallization (ELC) techniques, as shown in Fig. 2 (Hayashi et al., 1984; Sameshima et al., 1986).

The grain boundaries in poly-Si thin films typically feature random configurations. However, random grain boundaries were reported to severely degrade device performance (Blake et al., 1997). Therefore, grain enlargement is desirable. To achieve this, lateral growth during crystallization is necessary. The lateral growth described in this manuscript corresponds to oriented overgrowth of the crystalline film on a non-crystalline layer (i.e., the glass substrate), which is regarded as a type of epitaxy (Givargizov, 1991). Epitaxy proceeds so as to minimize the free energy and is expected to effectively reduce the defect density.

In this work, we investigate the relationship between lateral growth and defects using various characterization techniques. First, we give an overview the crystallization process on non-crystalline substrates and the characterization of defects in poly-Si thin films. Next, we describe previous studies and our work on SPC, ELC, and flow-shaped growth of poly-Si on glass from the perspective of lateral growth. Finally, the growth of a quasi-single-crystal SiGe thin film on a glass substrate, that is super-lateral growth, is demonstrated.

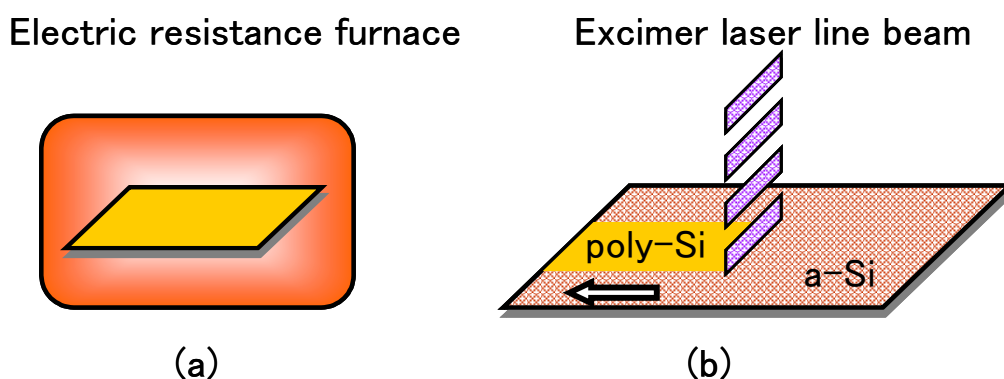


Fig. 2. Techniques for recrystallization of a-Si films on glass substrates using (a) solid-phase crystallization and (b) excimer-laser crystallization.

2. Overview of lateral crystallization on non-crystalline layer

The basic technology for poly-Si formation on a glass substrate is Si on insulator (SOI), which was developed for applications such as low power consumption large-scale integrated circuits (LSIs), three-dimensional LSIs, radiation-hardened electronics and solar cells. SOI technologies have been reviewed in detail elsewhere (Givargizov, 1991; Colinge, 2004). The substrate used for SOI is typically single-crystalline Si (c-Si) coated with a dielectric film such as SiO₂ or Si₃N₄. Although SOI technology includes a wide range of methods, we focus on the recrystallization of a-Si thin films. The principle SOI techniques used for this purpose are zone-melting recrystallization and lateral SPC.

Zone-melting recrystallization is performed by applying a heat source to an a-Si film, which induces melting followed by solidification of the film. Common heat sources are line-shaped electric resistors, electron beams, and continuous-wave (CW) Ar ion lasers. Lateral SPC is

also performed by zone heating; its advantages include low T_s (500–700 °C) and consistent surface smoothness.

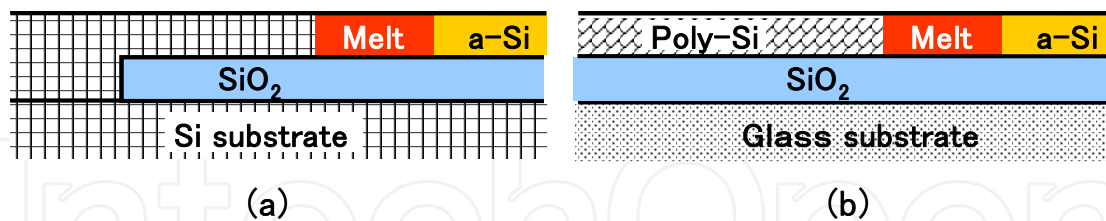


Fig. 3. Structures of Si layers on non-crystalline layers: (a) Si on insulator, where Si substrate is coated by SiO₂ film with windows for seed areas: (b) excimer-laser crystallized Si, where glass substrate is fully coated by SiO₂ film.

Control of nucleation during the initial stage of lateral growth and crystalline orientation is essential for the growth of single or quasi-single crystals. To achieve this control, the non-crystalline underlayer is partially opened to reveal the crystalline Si substrate, which acts as the seed area, as shown in Fig. 3(a). Alternatively, the fundamental layers are trenched in order to form a grating-like shape to guide the crystalline orientation; this is known as artificial epitaxy or graphoepitaxy. However, the structures thus created require additional photolithographic processing. In contrast, the laser crystallization process enables control of the crystalline orientation without seeding or photolithography; however, the obtained crystalline quality is not always adequate for the submicron-scale processes required for LSI.

For applications in electronic displays, the substrate should be glass or plastic rather than c-Si. On these substrates, Si thin films become essentially polycrystalline because of the seedless growth, as shown in Fig. 3(b). Poly-Si on glass has been applied in devices called giant microelectronics or large-area electronics (Kuriyama et al., 1992; Sameshima, 2009), which have areas several orders of magnitude larger than those of SOI devices. The use of glass or plastic substrates strongly restricts the upper limit of T_s . Technologies are classified as high-temperature poly-Si or low-temperature poly-Si depending on T_s (Blake, 1997). The border between them is determined by the strain point of a low alkali glass substrate at ~590 °C (Corning's technical glass catalog).

SPC requires a T_s that is higher than 600 °C. Thus, fused quartz glass is used as the substrate because its strain point is as high as 990 °C. SPC poly-Si is used mainly in 1-in. diagonal or smaller liquid crystal displays (LCDs) for multimedia projectors.

Laser crystallization technology decreases T_s to below the strain point of low alkali glass substrates and in many cases to room temperature (RT) owing to selective heating of the Si layer. Progress in laser annealing has been reviewed elsewhere (Sameshima, 2009). Poly-Si films for medium-sized LCD panels suitable for mobile information terminal applications have been formed.

There are two opposing requirements for laser crystallization: ensuring uniformity in order to integrate TFTs, and eliminating grain boundaries in order to improve the performance of individual TFTs. The former and latter requirements are met by the growth of grains that are notably smaller and larger than the TFT channels, as shown in Fig. 4(b) and 4(c), respectively. Those opposing needs are expected to be reconciled by the growth of flow-shaped grains, as shown in Fig. 4(d).

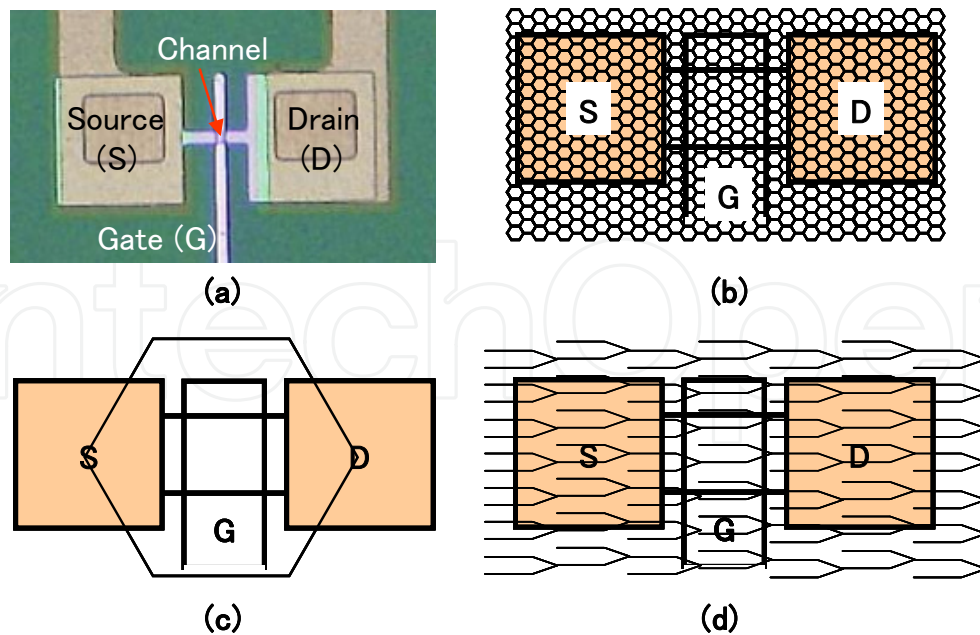


Fig. 4. Structures of thin-film transistors (TFTs) on glass substrates: (a) test device for characterizing electrical performance; geometry of grains and TFT channel for (b) grains notably smaller than the channel region, (c) a large grain containing the channel region, and (d) flow-shaped grains running parallel to the drain current.

3. Characterization of poly-Si films on glass

The principal terms for the characterization of poly-Si thin films on glass substrates are summarized in Table 1. The dangling bonds in a-Si and poly-Si films were qualitatively analyzed via the spin density of unpaired electrons using electron-spin resonance. The spin density was found to be reduced by hydrogenation (Nickel et al., 1997; Spinella et al., 1998), which causes termination of the dangling bonds with H atoms. The geometry and crystal orientation of the grains were investigated using images and diffraction patterns obtained by scanning electron microscopy (SEM), transmission electron microscopy (TEM), and electron backscattering diffraction (EBSD). When growth accompanies melting, the surface morphology can vary with the displacement of the melt. The surface morphology is observed using atomic force microscopy (AFM) or cross-sectional TEM. The electronic characteristics were estimated by fabricating test n-channel and p-channel TFT devices, as shown in Fig. 4(a). The devices exhibit characteristics such as the field-effect electron and hole mobilities ($\mu_{FE n}$ and $\mu_{FE p}$, respectively), threshold voltage, subthreshold voltage, and off-current.

The characterization techniques described above require the specimen be processed. Moreover, they are not simple enough to be used to characterize large numbers of films. In contrast, optical techniques are suitable for simple, non-destructive characterization. We analyzed the defects and stress in a poly-Si/glass system by Raman scattering spectroscopy (Kitahara et al., 2002, 2003, 2011a). Micro-Raman spectroscopy was conducted by using a Renishaw System 1000 in the backscattering geometry under excitation with a 514.5 nm Ar ion laser. Details of the setup and band component analysis were described elsewhere (Frost & Shurvell, 1997). The full width at half maximum (FWHM) values of spectra obtained for

poly-Si (described below) were calibrated according to the spectral resolution of the setup. The peak frequency of the spectra was exactly determined by fitting to a Lorentzian curve.

Typical first-order Raman scattering for c-Si, Si on sapphire (SOS), and poly-Si on glass are shown in Fig. 5. In the crystalline phase, the Raman spectrum exhibits an isolated band corresponding to the degeneration of a single transverse-optical (TO) phonon mode and two longitudinal-optical (LO) phonon modes; the c-Si band exhibits a linewidth as narrow as 2.5–3.5 cm⁻¹ at RT (Temple & Hathaway, 1973; Menendez & Cardona, 1984) owing to the $q = 0$ (q : wave vector) selection rule. In the amorphous phase, four continuous phonon bands are observed; they are broad because the $q = 0$ selection rule is loosened as a result of a decrease in the phonon correlation length.

The features of the optical phonon mode (OPM) of the crystalline phase are represented by the peak frequency (ω), FWHM, intensity, and in some cases asymmetry. When the grains are smaller than a few tens of nanometers, the spatial correlation of the phonon decreases, which causes the peaks to shift to a lower frequency ($\Delta\omega$) and increases the FWHM (Richter et al., 1981). Compressive and tensile stress in the films cause the peak to shift to higher and lower frequencies, respectively. Moreover, $\Delta\omega$ is proportional to the magnitude of the stress (Englet, 1980). Therefore, the stress can be quantitatively estimated only when the impact of the other factors is negligible. Note, however, that the intensity of the stress depends on the crystallization technique and conditions used. Therefore, an analysis of individual crystallization techniques should be developed by comparing the Raman spectroscopy results with those obtained by SEM and TEM.

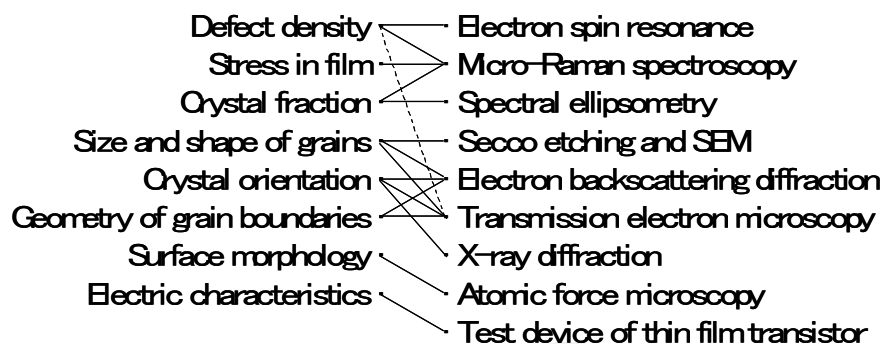


Table 1. Principal terms for characterization of poly-Si thin films on glass substrates.

Defects in poly-Si are frequently observed in SEM images. Grain boundaries and some defect clusters are clearly revealed by Secco etching (Secco d'Aragona, 1972). These defects are evidently electrochemically active, which is confirmed by the fact that they disappear upon hydrogenation before etching. On the other hand, inactive defects such as twin boundaries are observed only as shallow contrasts and are independent of hydrogenation (Kitahara et al., 2009a).

To summarize, various electron microscopies provide direct knowledge of defects and the geometric configuration of grains in poly-Si/glass systems. However, defects cannot always be detected by those methods. Raman microscopy is useful for easy macroscopic (submicron-scale) defect analysis and quantitative analysis of stress in films. However, semi-empirical analysis aided by other techniques is required to simultaneously characterize the defect density and stress in films by Raman spectroscopy.

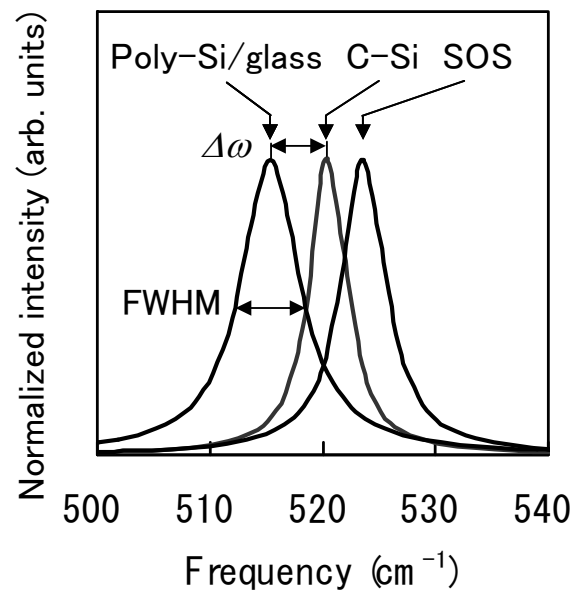


Fig. 5. Typical optical-phonon mode observed in the Raman scattering spectra for Si on sapphire (SOS), single crystalline Si (c-Si) bulk containing no stress, and poly-Si thin film on glass. Intensity is normalized to the individual peak values. Peaks are shifted to higher and lower frequencies by compressive and tensile stresses, respectively.

4. Solid-phase crystallization

The heat source for SPC typically consists of an electric resistance furnace and an infrared lamp annealing furnace. The force that drives crystallization of a-Si in the metastable state is the lowering of the Gibbs free energy through the crystalline phase change. SPC poly-Si technologies are reviewed in detail elsewhere (Hatalis & Greve, 1988; Spinella et al., 1998).

The typical grain size of solid-phase crystallized poly-Si for TFTs is a few hundred nanometers, which is at least several times larger than the film thickness. This suggests that SPC on non-crystalline substrates is dominated by lateral growth rather than columnar growth which is frequently seen in chemical vapor deposition.

SPC is initiated by homogeneous nucleation after incubation. In pure Si, the activation energy of nucleation is larger than that of growth by 0.25 eV (Spinella et al., 1998). Therefore, growth proceeds immediately after nucleation. The lower limit of the nucleation temperature depends on the quality of the precursor film and is ~ 560 °C for highly pure a-Si. The grain size decreases with increasing crystallization temperature (T_c), which is associated with increasing nucleation frequency. Lateral grain growth is first interrupted by collisions among grains. Then, the grain size increases due to secondary grain growth; the secondary growth rate increases with the grain boundary energy, surface energy anisotropy, grain boundary mobility, and T_c (Thompson, 1985). Furthermore, twin formation at the early stage of crystallization preferentially accelerates the lateral growth rate in the $\langle 112 \rangle$ direction, producing grains with an ellipsoidal outline (Nakamura et al., 1989). Growth along the minor axis of the ellipsoid, i.e., in the $\langle 111 \rangle$ direction, proceeds with simultaneous formation of many micro-twins (Drosed & Washburn, 1980). Although solid-phase crystallized poly-Si films have a considerable density of defects, hydrogenation of TFTs effectively inactivates those defects, producing a μ_{FEH} of 24 cm²/Vs (Little et al., 2001).

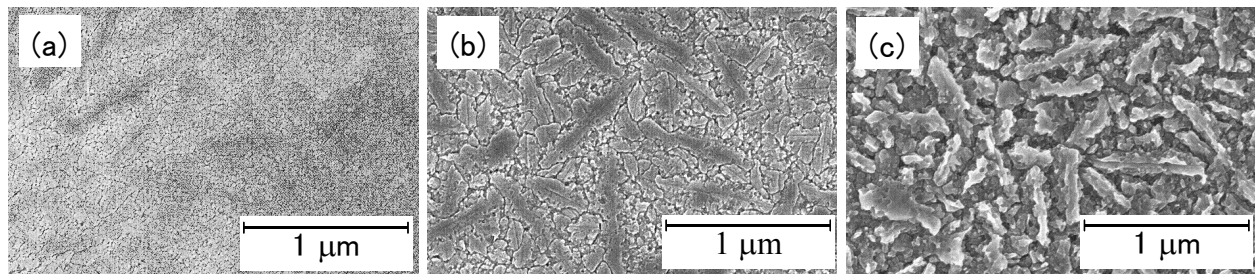


Fig. 6. Scanning electron microscopy images for solid-phase crystallized poly-Si heated at 900 °C for 1.5 h. Images were taken (a) before and after Secco etching for (b) 20 s and (c) 60 s.

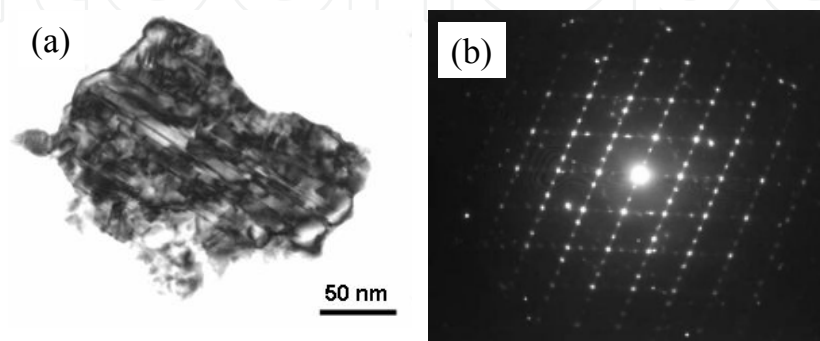


Fig. 7. Transmission electron microscopy image and diffraction pattern for solid-phase crystallized film heated at 900 °C for 3 h.

We investigated the microscopic geometry of the grains and defects by SEM and TEM. We then studied the phase variation at the initial stage macroscopically using Raman spectroscopy and spectroscopic ellipsometry. SPC was performed in a N₂ flow at atmospheric pressure. Figure 6 shows SEM images before and after Secco etching after SPC at $T_c = 900$ °C for 1.5 h. The surface of the as-crystallized film is relatively smooth. Grain boundaries were not clearly revealed by the short etching time (20 s) owing to the fine structures at the grain boundaries and the overlapping of grains (Spinella et al., 1998). The longer etching time (60 s) revealed feather-like grains lying parallel to the substrate. In addition, major twin boundaries appeared in the individual grains as shallow lines. The plan-view TEM image shown in Fig. 7 indicates that the twin boundaries extend along the major axis. Furthermore, a large density of micro-twins is distributed in the grains. The subspots and streaks evident in the diffraction pattern also indicate the presence of twins and {111} microfacets in the grains.

Figure 8 shows the OPMs in the Raman spectra during the initial stage of SPC at $T_c = 580$ °C. Only the amorphous phase is detected at 1 h. The crystal component begins to appear in the spectrum after a latent time of ~3 h. Figure 9 shows the crystal fraction in the 580 °C SPC film as a function of the heating time. In Raman spectroscopy, the volume fraction of the crystal was estimated by the area-intensity ratio of the amorphous (I_a) and crystal (I_c) components, i.e., $I_c/(I_c + I_a)$, which yields a relative value. In ellipsometry, the volume fraction of the crystal was analyzed using the Tauc-Lorentz model (Jellison, 1998), which yields an absolute value. Although no crystal component was found by Raman spectroscopy until 3 h had passed, the volume fraction estimated by ellipsometry began to increase at 1 h. The spectra of the imaginary dielectric function observed by ellipsometry show that the E1 and E2 bands were somewhat visible even in the latent time. This suggests that atomic

reconstruction toward ordering before the appearance of the crystal was detected by ellipsometry.

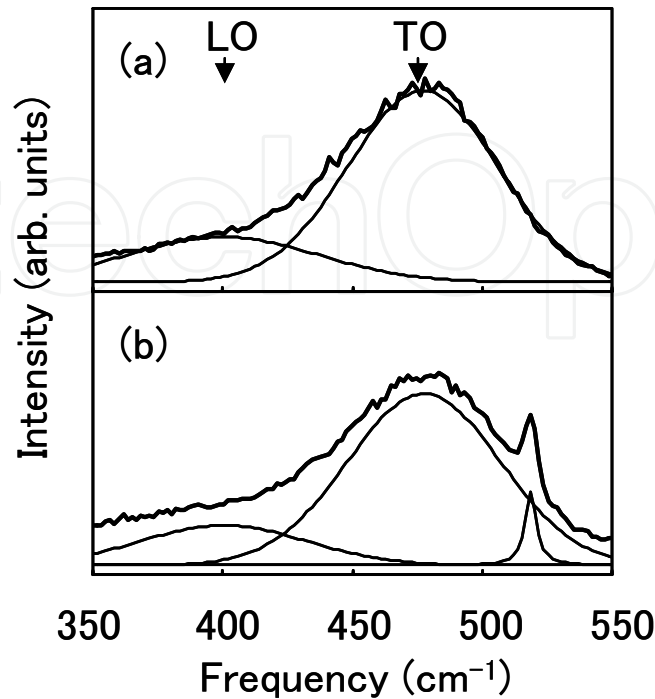


Fig. 8. Optical phonon modes in the Raman spectra for the initial stage of solid-phase crystallized film heated at 580 °C for (a) 1 h and (b) 3 h. Thick lines and thin lines are experimental values and fitting curves, respectively.

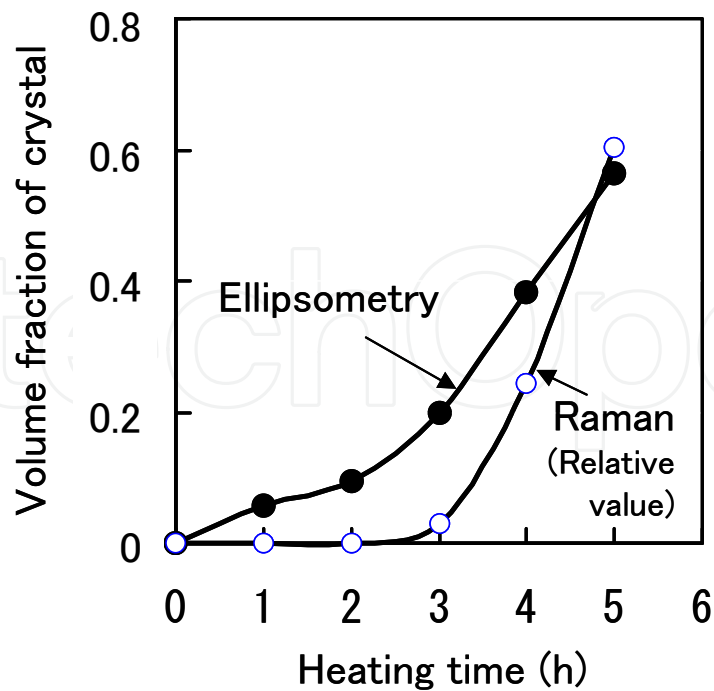


Fig. 9. Relationship between crystal fraction and heating time for solid-phase crystallized film heated at 580 °C. Crystal fraction was estimated using spectral ellipsometry and Raman spectroscopy.

Figure 10 shows the relationship between the FWHM of the OPM and T_c in the range of 625–900 °C with annealing times of 3–8 h; the times were varied in order to achieve sufficient crystallization. The FWHM evidently decreases with increasing T_c . Thus, the defect density decreases with increasing T_c , which is a universal tendency for crystal growth under essentially stable thermal equilibrium. The plots for metal-induced lateral crystallization (MILC) will be described in the next section.

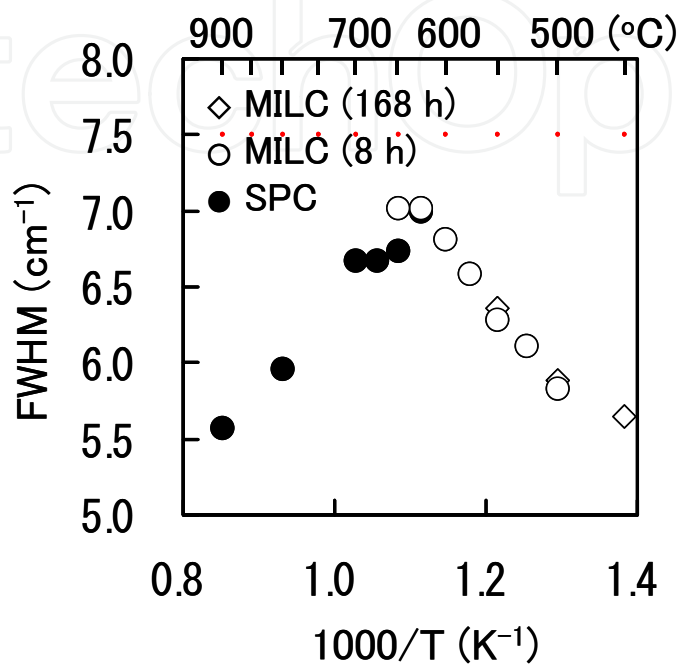


Fig. 10. Relationship between the full width at half maximum (FWHM) of the optical phonon mode and the crystallization temperature (T_c). Plots for poly-Si films fabricated by metal-induced crystallization (MILC) and solid-phase crystallization (SPC) are shown. Note that the dependence on T_c of MILC is opposite to that of SPC.

To summarize, Si atoms cause reconstruction toward ordering in the amorphous phase in the initial stage of annealing. SPC begins at homogeneous nucleations after the incubation time. Growth begins immediately after nucleation. The grain size increases with acceleration of lateral growth by the major twin boundaries formed at the early stage and the coalescence of grains by secondary grain growth. Growth proceeds with simultaneous formation of many micro-twins, resulting in many defects. Increasing T_c decreases the defect density in grains as the grain size is reduced.

5. Metal-induced lateral crystallization

The nucleation temperature of a-Si is decreased by the addition of a catalytic metal; the process is referred to as MILC and catalyst-assisted SPC (Kawatsu et al., 1990; Cammarata & Thompson, 1990; Takayama et al., 2000). Although metals such as Al, Mo, Ni, Pd, and Ti have been applied to cause MILC, Ni is the most frequently used catalyst. Ni can be supplied to the seed area of an a-Si film by evaporation, sputtering, or application of an acetate solution. Annealing of the film causes lateral diffusion of Ni atoms into the amorphous area before the silicide reaction occurs. NiSi_2 begins to segregate at $T_c > 420$ °C. Although NiSi_2 has the fluorite crystal structure, which is not the same as that of Si, the

mismatch of their lattice constants can be as small as 0.4%. Thus, NiSi₂ operates as an excellent nucleus for Si growth. NiSi₂ seeds then migrate laterally, leaving needle-like Si crystals in the a-Si. The activation energies reported for the growth rate of Ni-MILC, which range from 1.3–2.3 eV (Makihara et al., 2003; Kitahara et al., 2009b), are smaller than those for SPC (3.4 eV) and solid-phase epitaxy (2.7 eV) (Roth et al., 1990; Spinella et al., 1998). Lower values of T_c lead to straighter crystallization. Annealing at 450 °C reportedly results in crystals 10 μm in length and 160 nm wide (Makihara et al., 2003). Needle-like crystals coalesce and form larger grain when the remaining a-Si in the interstitial area is crystallized via SPC.

The application of MILC to devices is not easy because of the long processing time required and the existence of silicide in the crystallized region. However, TFTs have been fabricated by combining MILC with ELC. In this method, the silicide was gettered to ion-implanted regions corresponding to the source and drain electrodes and achieved a μ_{FEH} value of 320 cm²/Vs (Mizuki et al., 2004).

The density and geometry of the residual defects in MILC films are expected to differ from those in SPC films because MILC is more dominated by lateral growth than SPC is. We investigated the difference in defects between SPC and MILC (Kitahara et al., 2009b). MILC was performed by evaporating Ni onto an a-Si/SiO₂/fused quartz glass substrate through a metal mask with rectangular windows. The thicknesses of Ni and a-Si were 13 and 110 nm, respectively. The plan-view TEM image after MILC at 450 °C for 168 h is shown in Fig. 11(a). The image exhibits needle-like crystals with a {110} plane extending toward <111>. Note that the grains exhibited little contrast in the strain corresponding to defects. The coexistence of sharp diffraction spots and a halo in Fig. 11(a') indicate that the grain is a single crystal with a surrounding amorphous component. The TEM image after MILC at 500 °C for 168 h [Fig. 11(b)] shows accumulated needle-shaped grains with strain contrast due to defects. Small subspots in the diffraction pattern shown in Fig. 11(b') also indicate the presence of defects in the grains. However, the streaks corresponding to microfacets that were seen for the SPC films are not observed here. These results suggest that the number of defects in the grains decreases with decreasing T_c , which is opposite to the trend for SPC.

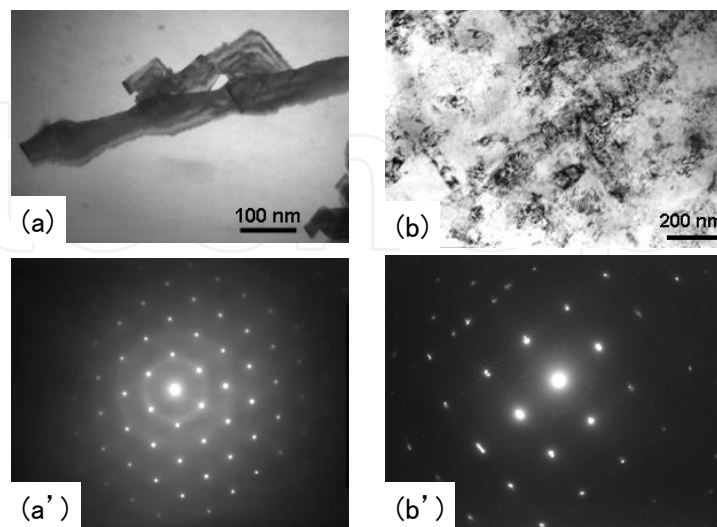


Fig. 11. Transmission electron microscopy images for (a) metal-induced crystallization (MILC) at 450 °C for 168 h and (b) MILC at 500 °C for 168 h. Individual diffraction patterns are also shown in (a') and (b').

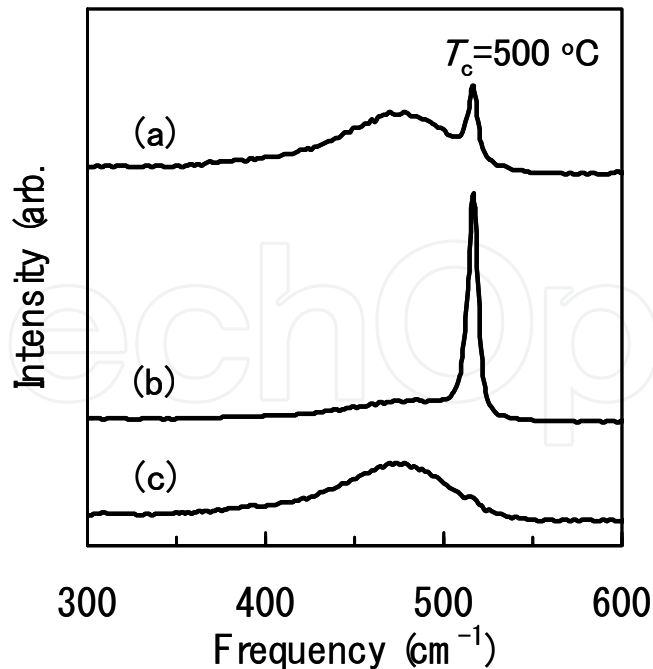


Fig. 12. Typical Raman spectra for (a) Ni-evaporated source region, (b) lateral growth region, and (c) uncrystallized region.

Typical Raman spectra for a Ni-evaporated source region, lateral growth region, and uncrystallized region are shown in Figs. 12(a)–(c). Here, MILC was conducted at 500 °C for 8 h. The spectrum for the Ni-evaporated region indicates the presence of a large amorphous fraction. In this area, the Ni density is likely too high to effectively induce lateral crystallization. In contrast, in the majority of the lateral growth region, the OPM is accompanied only by a weak amorphous-like mode. The uncrystallized region naturally remains amorphous. These results suggest that the amorphous-to-polycrystalline transition during MILC requires both a Ni supply and the lateral growth process.

The relationship between T_c and the FWHM of the OPM for the lateral growth region is shown in Fig. 10. The FWHM decreases with decreasing T_c and reaches 5.7 cm^{-1} at 450 °C, which is nearly equal to the FWHM of SPC at 900 °C, 5.6 cm^{-1} . A factor other than thermal energy is responsible for the T_c dependence of MILC because the dependence on T_c is opposite to that of SPC. In MILC, the Ni atoms exhibit a lateral gradation of density in a-Si due to diffusion from the source region. In particular, at $T_c < 500$ °C, the observed lateral growth length is smaller than the calculated Ni diffusion length in a-Si.

We concluded that the lateral growth at relatively low T_c is directed by the gradation in Ni density. Furthermore, the growth at T_c as low as 450 °C is dominated by needle-like lateral epitaxy and results in a low defect density. Increasing T_c restricts the length of straight growth and also enhances random growth due to SPC; these two effects increase the defect density despite the increase in T_c .

6. Excimer-laser crystallization

Crystallization is performed primarily by KrF or XeCl excimer lasers, which supply intense pulsed light with durations of ~ 30 ns and wavelengths of 249 and 308 nm, respectively. The

luminous flux is typically shaped as a linear beam. Overlapping irradiation by the scanning pulsed light enables uniform crystallization over a wide area. The laser energy density is adjusted to be slightly lower than that at which complete melting of the Si film occurs. In practical use, T_s is maintained at around RT during crystallization; this forms grains a few hundred nanometers in size with high reproducibility.

Because of the short pulse duration, T_s does not almost increase. However, rapid cooling after laser irradiation is an obstacle to lateral growth. Some techniques, including double-beam irradiation, have been proposed to decrease the cooling rate. Applying multiple laser irradiations at $T_s < 400$ °C reportedly increases the grain size to 4.5 μm and strongly aligns the surface orientation to the $\langle 111 \rangle$ direction (Kurimiya et al., 1993).

One of the features of ELC is a rough surface morphology containing a large density of hillocks. The hillocks are generated by a positive feedback effect between the beam-induced periodic surface roughness pattern and the interference in subsequent pulses (McCulloch & Brotherton, 1995). Another feature of ELC is that $\mu_{\text{FE}}^{\text{en}}$ is considerably higher than that of SPC. The $\mu_{\text{FE}}^{\text{en}}$ value of an excimer-laser crystallized poly-Si TFT increases with increasing grain size and reaches 320 cm^2/Vs at an average grain size of 700 nm, at which the dominant factor determining $\mu_{\text{FE}}^{\text{en}}$ varies from grain boundary scattering to lattice scattering (Hara et al., 2002a). Furthermore, a $\mu_{\text{FE}}^{\text{en}}$ value of 914 cm^2/Vs was reportedly obtained by position-controlled large grain growth (Mitani et al., 2008).

The large $\mu_{\text{FE}}^{\text{en}}$ value of excimer-laser crystallized poly-Si has been attributed to a low defect density in grains owing to a regrowth procedure through the liquid phase. In practice, TEM images typically exhibit few defects in the grains. The average dislocation density was reportedly $8 \times 10^6 \text{ cm}^{-2}$ for large (2–4 μm) grains and 10^8 – 10^9 cm^{-2} even for defective grains (Christiansen et al., 2001). However, the cooling velocity of ELC can be as high as $\sim 10^{10} \text{ K/s}$ (Sameshima & Usui, 1993). Therefore, recrystallization is expected to proceed under significant deviations from thermal equilibrium; consequently, large numbers of defects are frozen in the grains. In defects in bulk c-Si, impurity complexes generated at high temperature were shown to be frozen by quenching at a rate of $\sim 10^3 \text{ K/s}$ (Takahashi et al., 1995). The cooling rate of ELC is far larger than that in the quenching experiment. Hence, in ELC, defects undetectable by TEM are presumed to reside in the grains.

We studied defects in excimer-laser crystallized poly-Si (Kitahara et al., 2007, 2009a). We irradiated a-Si films (50 nm thick) on SiO_2 -coated fused quartz substrates with a XeCl excimer laser with 95% overlap. Figure 13 shows the surface of the excimer-laser crystallized poly-Si observed by SEM after Secco etching. Many hillocks appear as bright spots, as shown in Fig. 13(a); they are located at the junctions of grain boundaries. The hillock interval under the optimum conditions for ELC is nearly equal to the wavelength of the laser. AFM images indicated that ridges also lay along grain boundaries.

The grain boundaries were more evident after a longer etching time, as shown in Fig. 13(b). In contrast, grain boundaries did not appear in the hydrogenated film even after a long etching time, as shown in Fig. 13(c). This result implies that the grain boundaries were electrochemically inactivated by hydrogenation. On the other hand, structures other than grain boundaries were detected as shallow lines independently of hydrogenation, which could be due to the lack of electrochemically active dangling bonds.

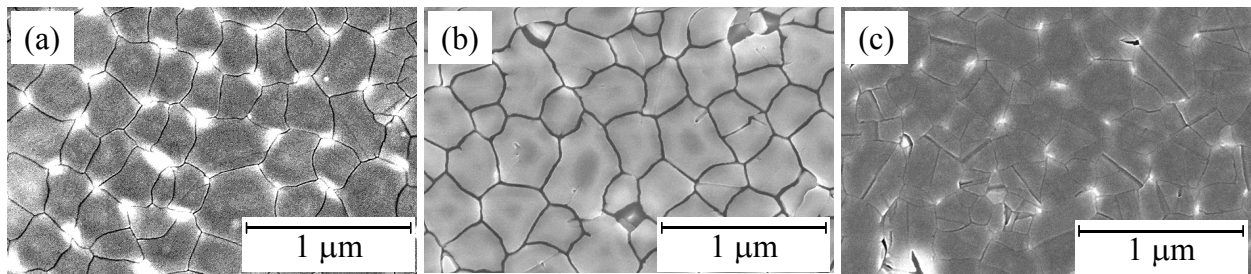


Fig. 13. Scanning electron microscopy images for (a, b) non-hydrogenated and (c) hydrogenated excimer-laser annealed poly-Si films. Secco etching was performed for (a) 15 s and (b, c) 40 s. Hydrogenation interfered with the appearance of grain boundaries after etching.

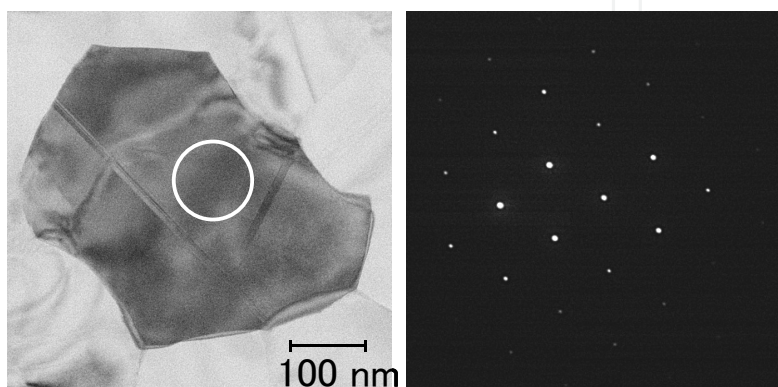


Fig. 14. Typical transmission electron microscopy image and diffraction pattern for a grain of excimer-laser crystallized poly-Si; diffraction pattern is that in the circled region..

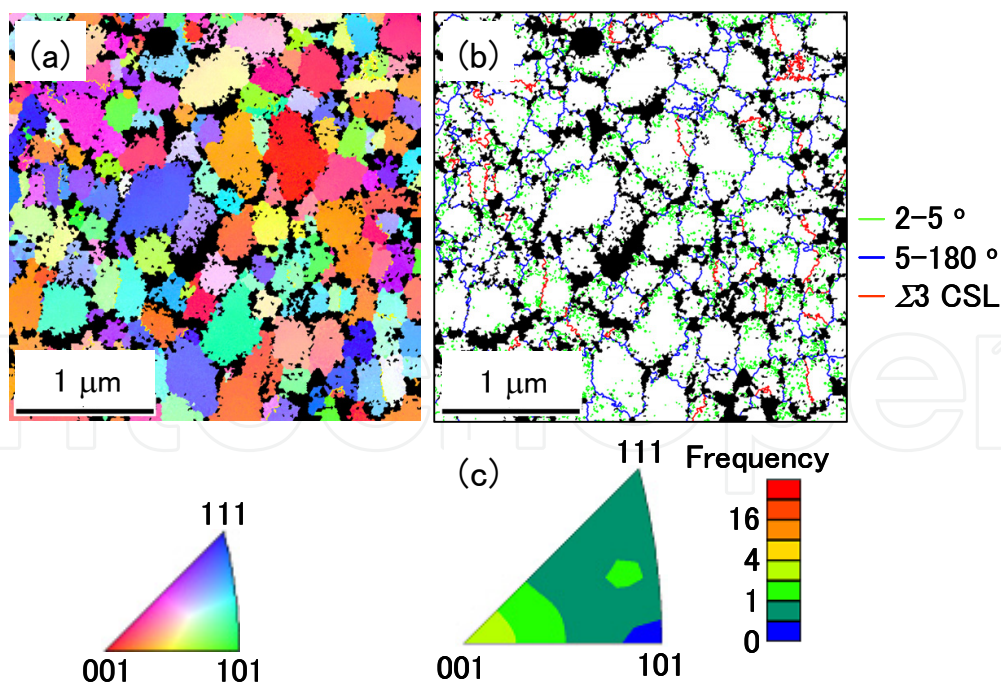


Fig. 15. (a) Crystalline orientation map in terms of the normal direction, (b) grain boundary map, and (c) inverse pole diagrams of the excimer-laser crystallized poly-Si, as observed by electron backscattering diffraction. Surface exhibits weak orientation to the $\{001\}$ plane. Twin boundaries appear for some grains.

A typical plan-view TEM image and diffraction pattern of a grain of excimer-laser crystallized poly-Si are shown in Fig. 14. The major twin boundary lies across the grain. However, unlike the results for SPC, no micro-twin was found in the grain. Dark contrast due to dislocation, defect clusters, and stacking faults tends to appear at the periphery of the grain.

The EBSD pattern of the surface normal direction (ND) is shown in Fig. 15. Although the surface orientation is scattered over a wide range, the {001} orientation has the highest frequency. A low index plane tends to exist owing to the small growth rate. The grain boundary map indicates that most grain boundaries are random and a quarter of the grains contain twin boundaries corresponding to the $\Sigma 3$ coincident-site lattice (CSL). The twin boundaries in other grains might be eliminated by grain coalescence due to secondary grain growth.

Raman spectroscopy was applied in order to obtain macroscopic and microscopic characterization of excimer-laser crystallized poly-Si. Figure 16 shows the variation in the FWHM and $\Delta\omega$ of the OPM with the energy density of the laser used for crystallization. The space correlation model (Richter et al., 1981) is useful for analysis of Raman spectra in order to deduce the decrease in the regularity of the crystalline structure, i.e., the presence of nanocrystals and large density defects. The relationship between the FWHM and $\Delta\omega$ of the OPM is plotted in Fig. 17, which also shows a line calculated using the space correlation model. The experimental plots exhibit the same tendency as the calculated values but are shifted to a lower frequency by $\sim 3 \text{ cm}^{-1}$. The magnitude of that deviation is close to the frequency shift caused by tensile stress in the film, which is induced by shrinkage of the film during solidification. The large values of both the FWHM and $\Delta\omega$ at low laser energies are due to the formation of nanosized crystals. At higher laser energies, the space correlation is determined by the defect density because the grains are sufficiently large. This suggests that the defect density is greater than 10^{12} cm^{-2} , which is estimated on the basis of the space correlation length deduced from the FWHM.

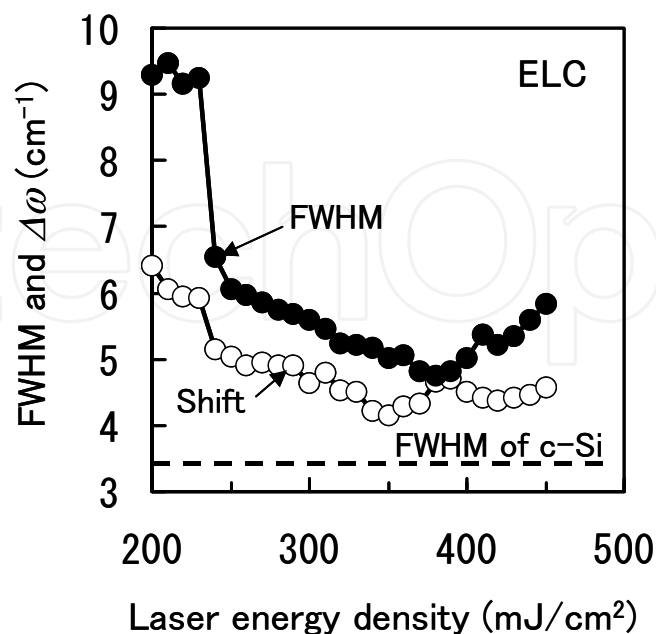


Fig. 16. Full width at half maximum (FWHM) and peak shift ($\Delta\omega$) of the optical-phonon mode as a function of the laser energy density used for crystallization.

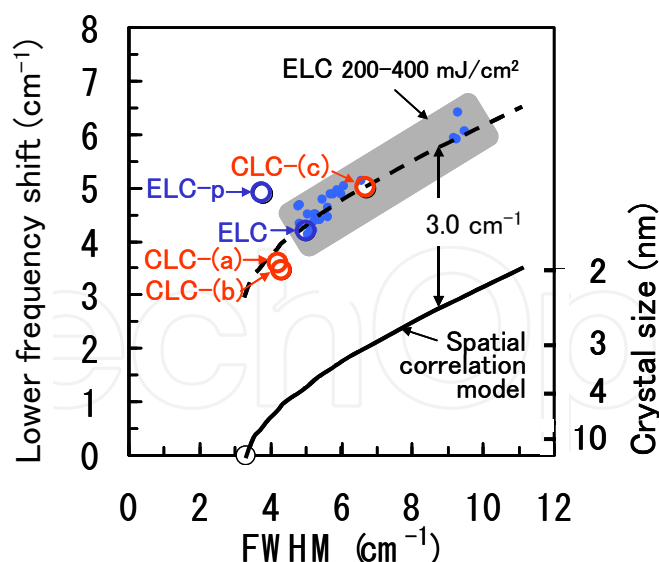


Fig. 17. Relationship between full width at half maximum (FWHM) and lower frequency shift ($\Delta\omega$) for excimer-laser crystallized poly-Si films irradiated at various energy densities. Plots for the film crystallized under the optimum conditions (excimer-laser crystallization, ELC) and that polished to remove hillocks and ridges on the surface (ELC-p) are also shown. Solid line is calculated from the space correlation model; broken lines are values shifted to larger $\Delta\omega$ by 3 cm^{-1} . Plots for continuous-wave laser lateral crystallization (CLC) will be described in the next section.

The Raman spectra for excimer-laser crystallized poly-Si exhibit remarkable features. For example, the intensity of Raman scattering is more than ten times that for SPC films with the same thickness and even that of bulk c-Si. This enhanced Raman scattering has been reported for a roughened semiconductor surface, Si nanocones, and Si nanotubes (Sridharan et al., 2003; Jayavel et al., 2006; Cao et al., 2006). Figure 18 shows a two-dimensional map of the OPM intensity for excimer-laser crystallized poly-Si. The observed area consists of a few micrometer-size grains enlarged by super-lateral growth (SLG) and nanocrystals adjacent to the SLG region (Im & Kim, 1993). The OPM intensity is clearly enhanced at grain boundaries. Thus, the large intensity for the excimer-laser crystallized films is attributed to the enhancement of Raman scattering by hillocks and ridges around the grain boundaries. Therefore, the Raman spectra of excimer-laser crystallized poly-Si reflect mainly the situation around grain boundaries. Accordingly, polishing the sample to remove the hillocks and ridges decreases the intensity to nearly one-tenth. Then, the Raman spectra begin to reflect the region inside the grain. The FWHM changes from 5.0 to 3.8 cm^{-1} after polishing. This supports the conclusion that Raman spectra of unpolished specimens reflect mainly the situation around grain boundaries, where the high defect density increases the FWHM.

The other feature of ELC is the hydrogenation effect. Excimer-laser crystallized poly-Si films with and without hydrogenation were examined in terms of the OPM. Figure 19 shows the variation in $\Delta\omega$ with Secco etching time; the results of SPC are also shown for comparison. The non-hydrogenated film exhibits relaxation of the tensile stress after a short etching period; the relaxation is due to penetration of the etching solution through clusters of defects in the grains to the poly-Si/SiO₂ interface. Defects inside the grain tend to accumulate rather than remain as point defects. In contrast, the hydrogenated excimer-laser

crystallized film exhibits almost no stress relaxation. Therefore, a large number of electrochemically active defects are assumed to be present in the grains even though they were not detected by TEM. In the solid-phase crystallized films and excimer-laser crystallized films annealed at 1000 °C, the reduction in stress with etching was not as abrupt, which implies that the thermal treatment reduced the number of dangling bonds in the grains.

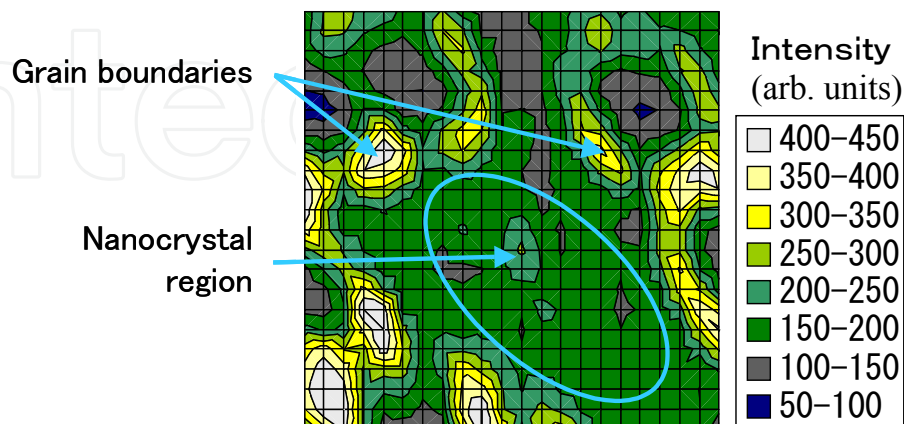


Fig. 18. Two-dimensional map of optical-phonon mode intensity for excimer-laser crystallized poly-Si consisting of a few micrometer-sized grains enlarged by super-lateral growth. View area is $4.2 \times 4.2 \mu\text{m}^2$. The intensity is apparently large at grain boundaries.

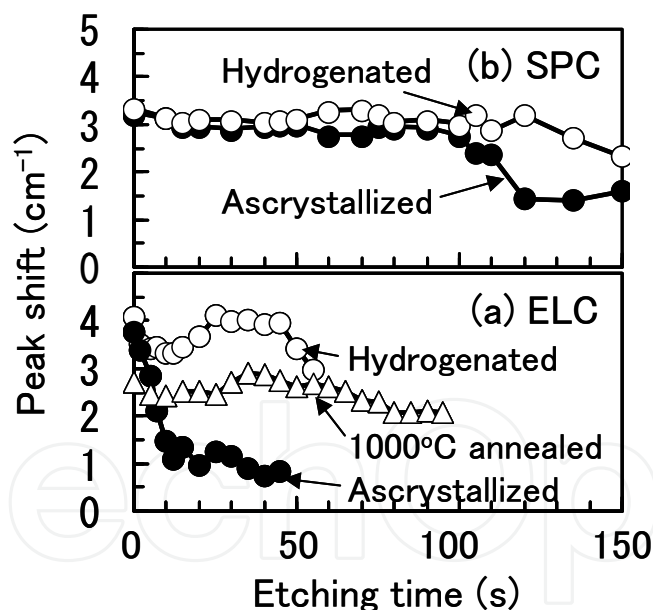


Fig. 19. Variation in peak shift with Secco etching time observed for (a) excimer-laser crystallization (ELC) and (b) solid-phase crystallization (SPC). Only the as-crystallized excimer-laser crystallized film exhibits a rapid decrease in the peak shift, which implies stress release in the film.

On the basis of the results shown above, ELC is considered to progress as follows. Excimer-laser irradiation under optimum conditions melts the film, leaving an adequate seed density. Because solidification occurs extremely quickly, a large number of defect clusters are frozen in the grains. Multiple irradiations affect the merging of relatively high-energy grains with

relatively low-energy grains. At a practical grain size of a few hundred nanometers, the lateral growth of individual grains at random orientation progresses, forming high-energy grain boundaries. A large number of the dangling bonds at grain boundaries and the accumulated defects in the grains are electrochemically and probably electronically active.

7. Flow-shaped growth

Free carriers in the channels of poly-Si TFTs are frequently scattered by grain boundaries. The presence of flow-shaped crystals aligned parallel to the channel current is expected to improve the electrical performance. The advantage of this configuration is that it does not require photolithography or complicated optical laser setup.

Flow-shaped growth of Si films has been achieved via techniques such as sequential-lateral solidification (SLS), selectively enlarging laser crystallization (SELAX), and CW laser lateral crystallization (CLC) (Im et al., 1997; Crowder et al., 2000; Hatano et al., 2002; Hara et al., 2002b; Fujii et al., 2007). SLS and SELAX employ pulsed excimer lasers and pulse-modulated diode-pumped solid-state (DPSS) CW lasers (a Nd:YVO₄ laser with a wavelength of 532 nm), respectively, as heat sources. In these methods, the region crystallized by the previous laser pulse acts as the seed for the next laser irradiation. Grain boundaries and subgrain boundaries run approximately parallel to the motion of the solidification interface. The general pattern consists of a branching river-like or wishbone structure (Crowder et al., 2000). The CLC procedure is based on the laser annealing method used in SOI technology. A compact CW DPSS laser or blue-ray semiconductor laser diode (Noguchi et al., 2010) is used as the heat source. Flow-shaped lateral growth is achieved by adjusting the laser scanning velocity and output power. TFTs fabricated by SELAX and CLC exhibit μ_{Fn} values of 440 and 566 cm²/Vs, respectively; these values are evidently larger than those of TFTs fabricated by conventional SPC and ELC.

We investigated the grain geometry and defects in grains produced by CLC (Kitahara et al., 2009a, 2011b). CLC was performed on 150 nm thick a-Si. Figure 20 shows SEM images of CW laser lateral crystallized poly-Si after Secco etching. The growth geometry varies from the center to the periphery of the laser beam and includes flow-shaped crystals, granular crystals, and leaf-shaped crystals extending to the periphery. The grain boundaries are distinctly visible as sharp etched lines. In the flow-shaped region, most of the etched lines were generated in the crystal, and the number of lines was diminished by coalescence with other lines. Lateral growth processes repeated the generation and reduction of boundaries, as in SLS. Note that the outlines of grains in the leaf-shaped region resemble those of the solid-phase crystallized poly-Si except for the length, which extends toward the outside of the beam. It is likely that the temperature gradient enhances lateral growth in SPC. Figure 20(a')-(c') show the surface of a hydrogenated specimen after Secco etching. Most of the grain boundaries in all regions became undetectable, which implies that they were electrochemically active.

Figure 21 shows the crystalline orientation maps and inverse pole diagrams of the Si film in terms of the ND and reference direction (RD) determined by EBSD; the RD is parallel to the laser scanning direction. The ND is distributed and tends to exhibit a high index, whereas the RD tends to be oriented toward $\langle 101 \rangle$ or $\langle 100 \rangle$. This suggests that the growth direction is stabilized by the liquid–solid interface rather than the surface or film–substrate interface. Many of the grains began to exhibit ND orientation to $\langle 100 \rangle$ with increasing film thickness

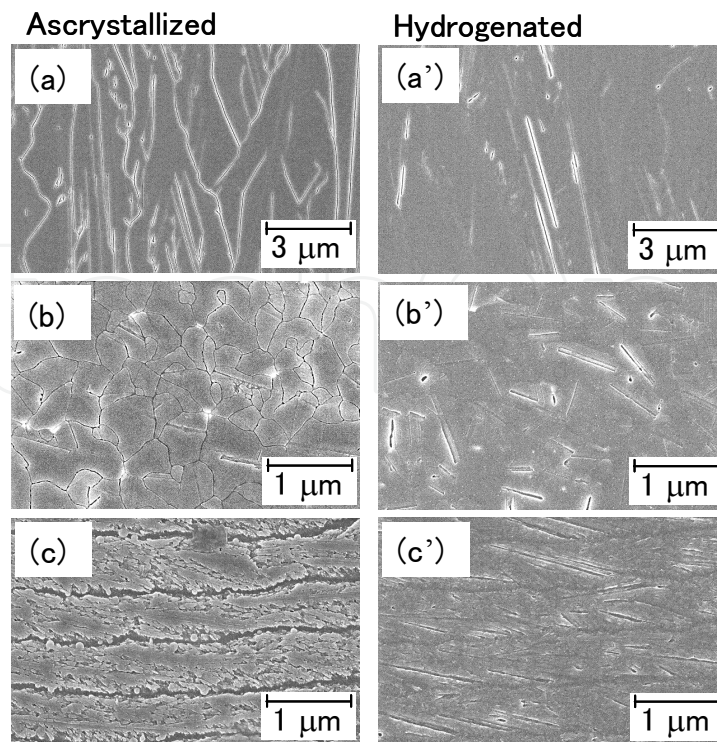


Fig. 20. Scanning electron microscopy images of continuous-wave laser lateral crystallized poly-Si. Secco etching was performed for 25 s. Observations were made in areas from the center to the periphery of the laser beam, as follows: (a) flow-shaped along the laser scanning direction, (b) granular, and (c) leaf-shaped extending to the periphery. (a')–(c') Images of the etched film after hydrogenation.

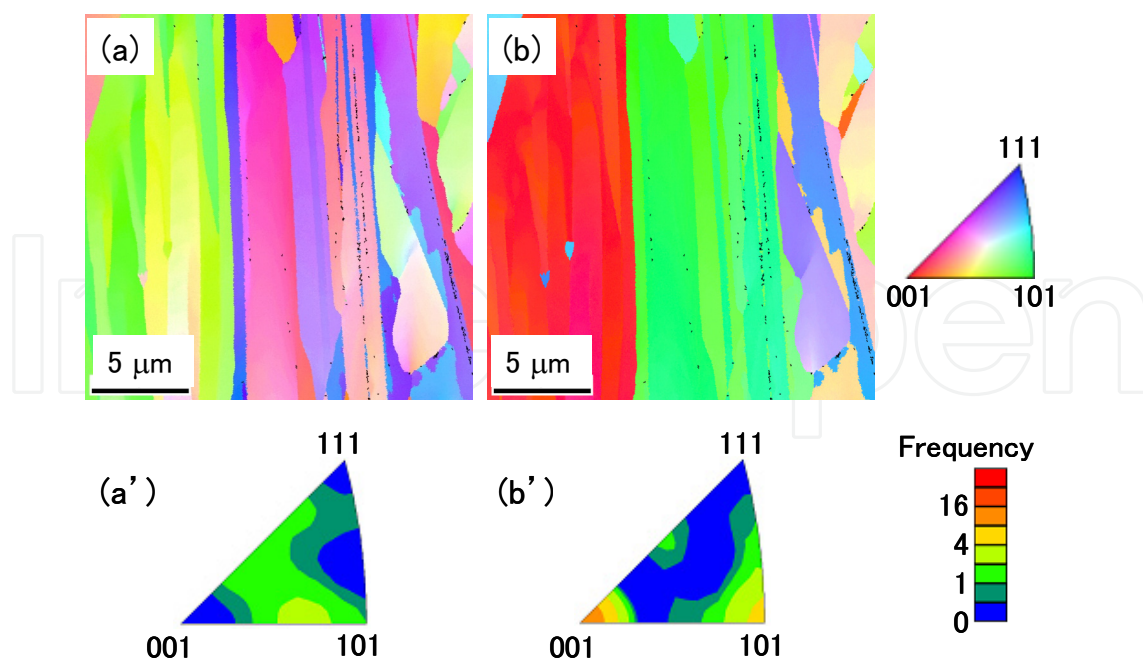


Fig. 21. Crystalline orientation maps for (a) normal direction and (b) reference direction and (a'), (b') individual inverse pole diagrams. Poly-Si film was formed by continuous-wave laser lateral crystallization.

(Hara et al., 2002b). The grain boundary map in Fig. 22(a) indicates that the $\Sigma 3$ CSL corresponding to the first-order twin boundary lies between the high-angle grain boundaries and extends in the laser scanning direction. Figure 22(b) shows the number fractions of the boundaries in terms of their misorientation angles. The $\Sigma 3$ CSL with a tilt angle of 60° occupies a fraction of ~ 0.4 . First-order twin boundaries reportedly are not electrically active, whereas second-order twin boundaries act as strong recombination centers (Cunningham et al., 1982). Therefore, the present $\Sigma 3$ CSL is regarded as electrically inactive. The remaining boundaries, which occupy a fraction of ~ 0.6 , are distributed over a wide range of angles.

Figure 17 shows the relationship between the FWHM and $\Delta\omega$ for three regions in the CW laser lateral crystallized film: (a) flow-shaped growth, (b) granular growth, and (c) SPC-like growth. Regions (a) and (b) exhibit very similar FWHM and $\Delta\omega$ values, which are somewhat smaller than those obtained by ELC. The difference between CLC and ELC can be attributed to the cooling rate. That of CLC is three to four orders of magnitude smaller than that of ELC; the cooling rate of ELC is determined by the scan speed and energy gradation at the edge of the laser beam.

As described above, flow-shaped crystals were successfully grown by CLC. The crystalline boundaries in the resulting films, except for the $\Sigma 3$ CSL, are electrochemically active, like those of excimer-laser crystallized films. The defect cluster density in the grains of the CW laser lateral crystallized films is smaller than that of the excimer-laser crystallized films; this is explained by the fact that the cooling rate of CLC is several orders of magnitude smaller than that of ELC.

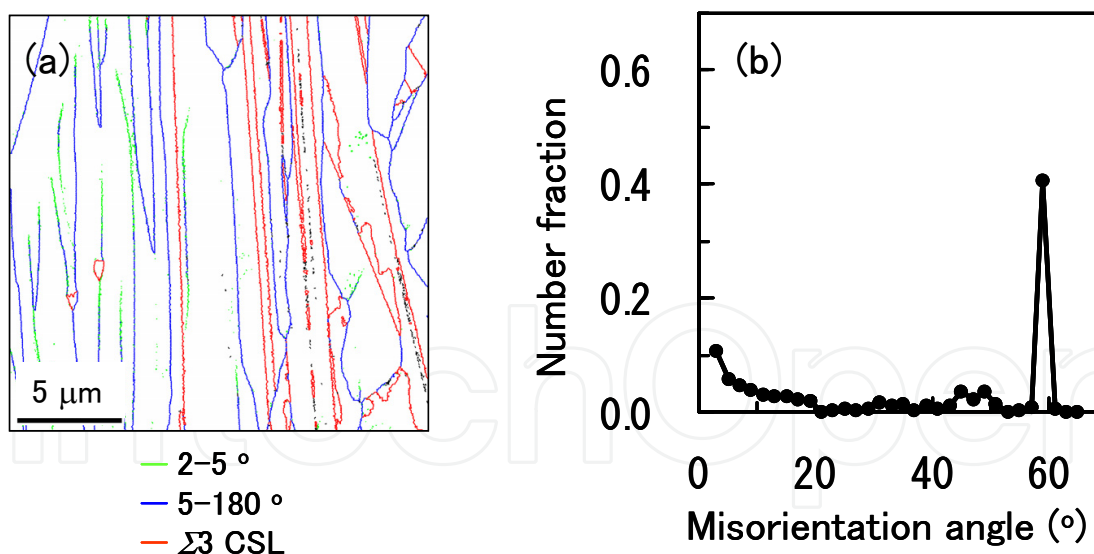


Fig. 22. (a) grain boundary maps and (b) number fractions of the boundaries in terms of the misorientation angle for the poly-Si films shown in Fig. 21. $\Sigma 3$ coincident site lattice dominates the boundaries.

8. Growth of quasi-single crystalline SiGe thin films

Compounding Si with germanium (Ge) not only extends the application of band engineering but also reduces the melting point, which is advantageous for growth on glass

substrates. Rapid melt growth on sapphire substrates and ELC on glass substrates have been reported as techniques for the growth of SiGe thin films (Sameshima et al., 2005; Weizman et al., 2005; Koh et al., 2010; Tanaka et al., 2010). Strong lateral segregation reportedly caused the local Ge content to differ by as much as 40% from the average value (Weizman et al., 2005). Therefore, it is necessary to examine the segregation of Ge and the appropriate growth mode for alloys in order to form crystalline SiGe on glass substrates.

We investigated the crystal configuration, Ge segregation, and growth modes specific to the alloy (Kitahara et al., 2011b). SiGe thin films were crystallized on glass substrates using CLC with a DPSS CW laser. The precursor film was amorphous $\text{Si}_{0.7}\text{Ge}_{0.3}$ with a thickness of 100 nm.

A typical Raman spectrum of the $\text{Si}_{0.7}\text{Ge}_{0.3}$ film is shown in Fig. 23. The crystallization of the SiGe films was confirmed by the appearance of sharp optical phonon modes at $\sim 300\text{ cm}^{-1}$ for the Ge-Ge bond, $\sim 400\text{ cm}^{-1}$ for the Si-Ge bond, and $\sim 500\text{ cm}^{-1}$ for the Si-Si bond.

Figure 24 shows a reflection electron image. In the region corresponding to the central position of the laser beam, multiple areas of bright contrast that extend for more than $100\text{ }\mu\text{m}$ run parallel to the laser scanning direction at intervals of $\sim 1\text{ }\mu\text{m}$. The coalescence and generation of grain boundaries observed in pure Si films were not evident here, which indicates a type of super-lateral growth. Because the reflection electron intensity depends on the atomic number, the contrast suggests strong segregation of Ge along the bright lines.

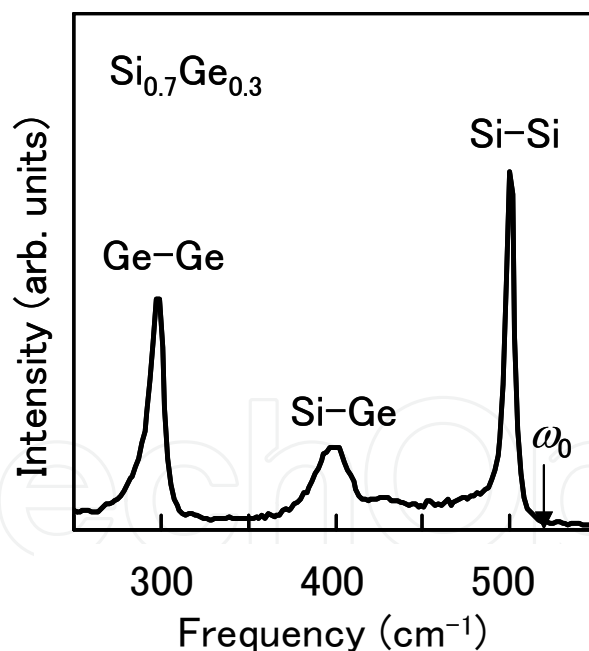


Fig. 23. Typical Raman spectrum for the optical phonon modes of Ge-Ge, Si-Ge, and Si-Si bonds in a crystallized $\text{Si}_{0.7}\text{Ge}_{0.3}$ film. Peak position for unstrained Si is indicated by ω_0 . The lower shift of the Si-Si band from ω_0 depends primarily on the Ge content.

Figure 25 shows crystalline orientation maps and inverse pole diagrams of the film determined by EBSD. "ND" indicates that the crystals are strongly aligned with the $\langle 111 \rangle$ plane. The RD, which corresponds to the laser scanning direction, tends to align with the $\langle 101 \rangle$ plane. Figure 26 shows the grain boundary map and number fractions of boundaries

in terms of their misorientation angles. The map shows that there were very few high-angle grain boundaries. Twin islands were aligned parallel to the laser scanning direction and were outlined by the $\Sigma 3$ CSL. Although low-angle grain boundaries with a misorientation of $<5^\circ$ appeared, their population was relatively small. Thus, these findings indicate that a quasi-single crystal was formed in the film.

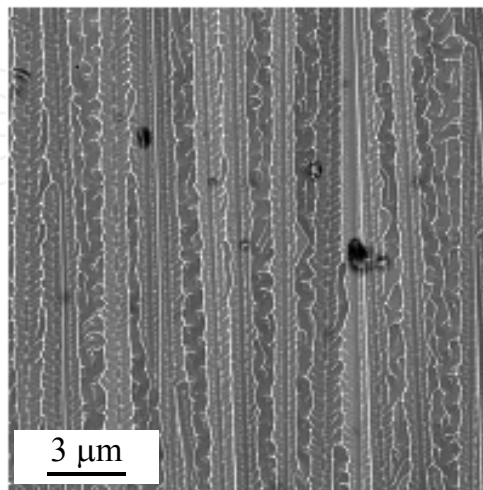


Fig. 24. Reflection electron image of the surface of the Si_{0.7}Ge_{0.3} film. Bright areas corresponds to regions of Ge accumulation.

Figure 27 shows a TEM image and an energy-dispersive X-ray (EDX) profile of Si and Ge. Multiple areas of dark contrast run nearly parallel to the laser-scanning direction in the TEM image. The EDX profile indicates that Ge is strongly segregated in the dark regions of the TEM image. This finding is consistent with the Ge segregation estimated from the reflection electron image in Fig. 24. Thus, Ge segregation was found to occur at many $\Sigma 3$ CSLs and at both low- and high-angle grain boundaries.

The $\Sigma 9$ CSL for pure Si reportedly can construct a dangling-bond-free stable structure through the formation of 5- and 7-membered rings (Kohyama & Yamamoto, 1994). In SiGe alloys, the energy at the boundaries can be further reduced by locally varying the Ge content and thus adjusting the lattice constant.

The alloy's characteristics should be considered when discussing the proper growth of SiGe. In pure materials, the solid-liquid interface under a positive temperature gradient is essentially flat during solidification. In contrast, the solid phase in alloys extends into the melt owing to the instability of the solid-liquid interface, resulting in oriented cellular growth; this corresponds to the constitutional undercooling model (Chalmers, 1964). Si and Ge form a complete solid solution. From the phase diagram and the calculation of the equilibrium partition coefficient, the undercooled area was estimated to be on the order of submicrometers in front of the growth region (Kitahara et al., 2011b).

As described above, the growth mode of CLC was changed from flow-shaped growth to super-lateral growth by compounding Ge with Si. This result was attributed to the constitutional undercooling that is peculiar to alloys. At crystalline boundaries running along the laser scanning direction, the energy was lowered by Ge segregation, resulting in the suppression of high-angle grain boundaries. As a result, quasi-single-crystalline films were formed on glass substrates.

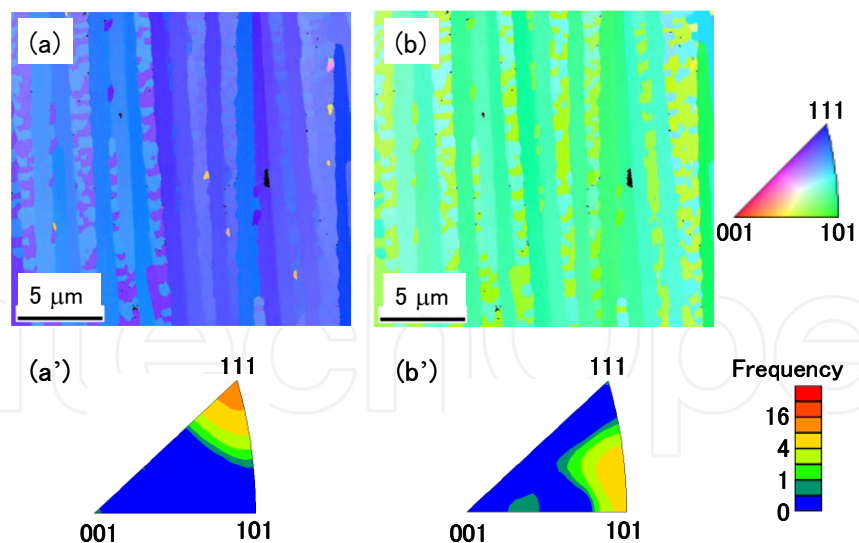


Fig. 25. Crystal orientation maps and inverse pole diagrams for (a, a') normal direction and (b, b') reference direction of $\text{Si}_{0.7}\text{Ge}_{0.3}$ film. Surface is strongly oriented to $\langle 111 \rangle$.

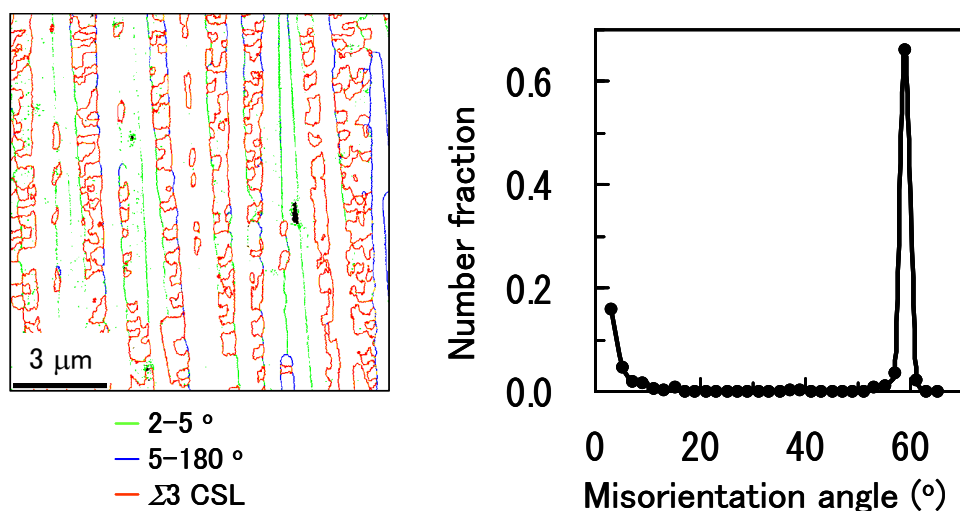


Fig. 26. Grain boundary map and number fractions of the boundaries in terms of the misorientation angle for $\text{Si}_{0.7}\text{Ge}_{0.3}$ film. Boundaries consist mainly of $\Sigma 3$ coincident site lattice.

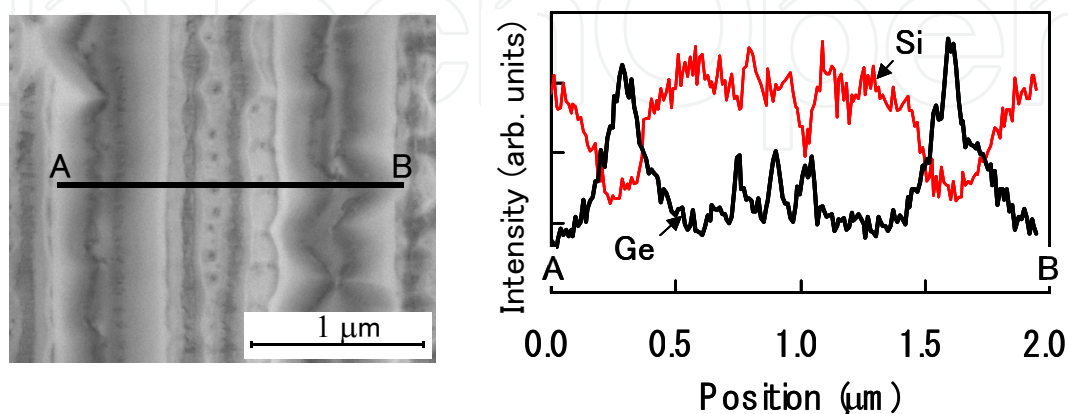


Fig. 27. Transmission electron microscopy image and electron dispersion X-ray profile of Si and Ge atoms in crystallized $\text{Si}_{0.7}\text{Ge}_{0.3}$ film. Profiles were taken between A and B in the image.

9. Conclusions

Lateral crystallization is indispensable for the growth of poly-Si films on glass substrates for application in large-area devices such as electronic displays and solar cells. In this paper, an outline of the various crystallization techniques was introduced, and our study of lateral growth and defects was described.

When SPC was used, lateral growth proceeded along the major twin boundary. However, a large density of micro-twins appeared in the grains. Oriented lateral growth is expected to decrease the number of defects. In practice, MILC exhibited a decreased defect density with lowered growth temperature, which is attributed to enhanced directivity of needle-like growth.

In ELC, growth is accompanied by melting and recrystallization of the film. TEM revealed only low-density defects in grains. Those defects consisted primarily of dislocations. However, Raman spectroscopy and chemical etching indicated the presence of a considerable density of defects in the grains and at the grain boundaries. The existence of defects in the grains was attributed to the high cooling velocity during recrystallization.

CLC is advantageous for its low cooling velocity and ability to produce oriented lateral growth. Relatively small defect densities were observed in pure Si films. Lateral growth proceeds by generation and disappearance of sub-grain boundaries along the laser scanning direction. Lateral growth was significantly enhanced by compounding Ge with Si, which results in a type of super-lateral growth. Such growth was attributed to the constitutional undercooling effect that is characteristic of alloys. The undercooling effect and the segregation of Ge decrease the energy at the boundaries running parallel to the laser scanning direction, resulting in the growth of quasi-single-crystalline films on glass.

Not only Si and Si-related films but also metal oxides and organic films are beginning to be extensively developed as materials for electronic devices on glass or plastic films. Si will share this role in the development of high-performance devices. One of the remarkable achievements of Si technology is the growth of single-crystalline films on large-area substrates, although such films suffer from cracking, which must be avoided in heterostructures. Both the advance of laser technologies and the control of the physical properties of materials, such as alloying and stacking of different layers, are more promising for the growth of single-crystal films on non-crystalline substrates.

10. Acknowledgements

The authors would like to thank Prof. Tsuda H. in Osaka Prefecture Univ. for TEM observation of SPC and MILC poly-Si. This study was funded in part by the Japan Society for the Promotion of Science [Grants-in-Aid for Scientific Research, (B) 19360165 and (C) 21560329].

11. References

Blake, J. G.; King, M. C.; Stevens III, J. D. & Young R. (1997). Low-Temperature Polysilicon Reshapes FPD Production, *Solid State Technology*, Vol, 40, No. 151, pp. 151-161

- Cammarata, R. C.; Thompson, C. V.; Hayzelden, C & Tu, K. N. (1990). Silicide Precipitation and Silicon Crystallization in Nickel Implanted Amorphous Silicon Thin Films, *Journal of Materials Research*, Vol. 5, No. 10, (October 1990), pp. 2133-2138
- Cao, L.; Nabet, B. & Spanier, J. E. (2006), Enhanced Raman Scattering from Individual Semiconductor Nanocones and Nanowires, *Physical Review Letters*, Vol. 96 (April 2006), pp. 157402-1-4.
- Chalmers, B. (1964). *Principles of Solidification*, John Wiley and Sons Inc., New York
- Christiansen, S.; Lengsfeld, P.; Krinke, J.; Nerding, M.; Nickel, N. H. & Strunk, H. P. (2001). Nature of Grain Boundaries in Laser Crystallized Polycrystalline Silicon Thin Films, *Journal of Applied Physics*, Vol. 89, No. 10 (May 2001), pp. 5348-5354
- Crowder, M. A.; Limanov, A. B. & Im J. S. (2000). Sub-Grain Boundary Spacing in Directionally Crystallized Si Films Obtained via Sequential Lateral Solidification, *Materials Research Society Symposium Proceedings*, Boston, 2000, Vol. 621, pp. Q9.6.1-Q9.6.6
- Colinge, J.-P. (2004). *Silicon-on-Insulator Technology: Materials to VLSI*, Springer, New York, ISBN: 1-4020-7773-4
- Cunningham, B.; Strunk, H. & Ast, D. G. (1982). First and Second Order Twin Boundaries in Edge Defined Film Growth Silicon Ribbon, *Applied Physics Letters*, Vol. 40, No. 3 (February 1982), pp. 237-239
- Drosed, R. & Washburn, J. (1980). A New Technique for Observing the Amorphous to Crystalline Transformation in Thin Surface Layers on Silicon Wafers, *Journal of Applied Physics*, Vol. 51, No. 8 (August 1980), pp. 4108-4110, ISSN 0021-8979
- Englert, Th.; Abstrerer, G. A.; & Pontcharra, J. (1980). Determination of Existing Stress in Silicon Films on Sapphire Substrate Using Raman Spectroscopy, *Solid-State Electronics*, Vol. 23, pp. 31-33
- Frost R. L. & Shurvell H. F. (1997). Raman Microprobe Spectroscopy of Halloysite, *Clays and Clay Minerals*, Vol. 45, No. 1, pp. 58-72
- Fujii S., Kuroki S., Kotani K. & Ito T. (2007). Enlargement of Crystal Grains in Thin Silicon Films by Continuous-Wave Laser Irradiation, *Japanese Journal of Applied Physics*, Vol. 46, No. 4B (April 2007), pp. 2501-2504
- Givargizov, E. I. (1991). *Oriented Crystallization on Amorphous Substrate*, Premium Press, New York, ISBN: 0-306-43122-X
- Hara, A.; Takeuchi, F. & Sasaki, N. (2002a). Mobility Enhancement Limit of Excimer-Laser-Crystallized Polycrystalline Silicon Thin Film Transistors, *Journal of Applied Physics*, Vol. 91, No. 2, (January 2002) pp. 708-714, ISSN 0021-8979
- Hara, A.; Takeuchi, F.; Takei, M.; Suga, K.; Yoshino, K.; Chida, M.; Sano, Y. & Sasaki, N. (2002b). High Performance Polycrystalline Silicon Thin Film Transistors on Non-Alkali Glass Produced Using Continuous Wave Laser Lateral Crystallization, *Japanese Journal of Applied Physics*, Vol. 41, Part 2, No. 3B, (March 2002), pp. L311-L313
- Hatalis, M. K. & Greve, D. W. (1988). Large Grain Polycrystalline Silicon by Low-Temperature Annealing of Low-Pressure Chemical Vapor Deposited Amorphous Silicon Films, *Journal of Applied Physics*, Vol. 63, No. 7, (April 1988), pp. 2260-2266, ISSN 0021-8979

- Hatano, M.; Shiba, T. & Ohkura, M. (2002). Selectively Enlarging Laser Crystallization Technology for High and Uniform Performance Poly-Si TFTs, *SID Symposium Digest of Technical Papers*, Boston, May 2002, Vol. 33, Issue 1, pp. 158-161
- Hayashi, H.; Noguchi, T. & Oshima, T. (1984). Polysilicon Super-Thin Film Transistor (SFT), *Japanese Journal of Applied Physics*, Vol. 23, No. 11, (November 1984), L819-L820
- Im, J. S. & Kim, H. J. (1993). Phase Transformation Mechanisms Involved in Excimer Laser Crystallization of Amorphous Silicon Films, *Applied Physics Letters*, Vol. 63, No. 14, (October 1993), pp. 1969-1971, ISSN 0003-6951
- Im, J. S.; Sposili, R. S. & Crowder, M. A. (1997). Single-Crystal Si Films for Thin-Film Transistor Devices, *Applied Physics Letters*, Vol. 70, No. 25, (June 1997), pp. 3434-3436, ISSN 0003-6951
- Jayavel, P.; Nakamura, S.; Kesavamoorsly, R.; Srivastava, G. P.; Tomoda, W.; Koyama, T. & Hayakawa, Y. (2006). Surface Morphology Effects on the Optical Phonon Modes in InAs_xSb_{1-x} Epilayers on GaAs(001), *Physica Status Solidi (b)*, Vol. 243, No. 4, (February 2006), pp. R19-R21
- Jellison, Jr. G. E. (1998). Spectroscopic Ellipsometry Data Analysis: Measure Versus Calculated Quantities, *Thin Solid Films*, Vol. 313-314, (February 1998), pp. 33-39, ISSN 0040-6090
- Kawazu, T.; Kudo, H.; Onari, S. & Arai, T. (1990). Low-Temperature Crystallization of Hydrogenated Amorphous Silicon Induced by Nickel Silicide Formation, *Japanese Journal of Applied Physics*, Vol. 29, No. 12, (December 1990), pp. 2698-2704
- Kitahara, K.; Yamazaki, R.; Kurosawa, T.; Nakajima, K. & Moritani, A. (2002). Analysis of Stress in Laser-Crystallized Polysilicon Thin Films by Raman Scattering Spectroscopy, *Japanese Journal of Applied Physics*, Vol. 41, Part 1, No. 8, (August 2002), pp. 5055-5059
- Kitahara, K.; Ohnishi, K.; Katoh, Y.; Yamazaki, R. & Kurosawa, T. (2003). Analysis of Defects in Polycrystalline Silicon Thin Films Using Raman Scattering Spectroscopy, *Japanese Journal of Applied Physics*, Vol. 11, Part 1, No. 11, (November 2003), pp. 6742-6747
- Kitahara, K.; Ohashi, Y. & Matsumoto, S. (2007). Hydrogenation Effects on Chemical Activity of Defects in Excimer-Laser-Annealed Polycrystalline Silicon Thin Films, *Japanese Journal of Applied Physics*, Vol. 46, No. 19, (May 2007), pp. L448-L450
- Kitahara, K.; Ohashi, Y.; Yamamoto, K. & Sasaki, N. (2009a). Electrochemical and Raman-Scattering Characterizations of Defects in Polycrystalline Silicon Thin Films Formed by Excimer-Laser Annealing, Solid-Phase Crystallization, and Continuous-Wave Lateral Crystallization, *Japanese Journal of Applied Physics*, Vol. 48, (February 2009), pp. 021205 (6 pages)
- Kitahara, K.; Kambara, J.; Kobata, M. & Tsuda, H. (2009b). Suppression of Defects during Metal-Induced Lateral Crystallization of Polycrystalline-Silicon Thin Films by Directed Lateral Growth, *Japanese Journal of Applied Physics*, Vol. 48, pp. 091203 (5 pages)
- Kitahara, K.; Ishii, T.; Suzuki, J.; Bessyo, T.; Watanabe, N. (2011a). Characterization of Defects and Stress in Polycrystalline Silicon Thin Films on Glass Substrates by Raman Microscopy, *International Journal of Spectroscopy*, Vol. 2011, (August 2011), pp. 632139 (14 pages), doi:10.1155/2011/632139
- Kitahara, K.; Hirose, K.; Suzuki, J.; Kondo, K. & Hara, A. (2011b) Growth of Quasi-Single-Crystal Silicon-Germanium Thin Films on Glass Substrates by Continuous Wave

- Laser Lateral Crystallization , *Japanese Journal of Applied Physics*, Vol. 50, (October 2011), pp, 115501 (6 pages)
- Koh, H.-Y. S.; Chen, S.-L.; Griffin, P. B. & Plummer, J. D. (2010). High Quality Single-Crystal Laterally Graded SiGe on Insulator by Rapid Melt Growth, *Electrochemical and Solid State Letters*, Vol. 13, Issue 8, (May 2010), pp. H281-H283
- Kohyama, M. & Yamamoto, R. (1994). Theoretical Study of Grain Boundaries in Si: Effects of Structural Disorder on the Local Electronic Structure and the Origin of Band Tails, *Physical Review B*, Vol. 50, No. 12, (September 1994), pp. 8502-8522, ISSN 0163-1829
- Kuriyama, H.; Kuwahara, T.; Ishida, S.; Nohda, I.; Sano, K. & Iwata, H. (1992). Improving the Uniformity of Poly-Si Films Using a New Excimer Laser Annealing Method for Giant- Microelectronics, *Japanese Journal of Applied Physics*, Vol. 31, Part 1, No. 12B, (December 1992), pp. 4550-4554
- Kuriyama, H.; Nohda, T.; Ishida, S.; Kuwahara, T.; Noguchi, S.; Kiyama, S.; Tsuda, S. & Nakano, S. (1993). Lateral Grain Growth of Poly-Si Films with a Specific Orientation by an Excimer Laser Annealing Method, *Japanese Journal of Applied Physics*, Vol. 32, Part 1, No. 12B, (December 1993), pp. 6190-6195
- Little, T. W.; Takahashi, K.; Koide, H.; Nakazawa, T.; Yudasaka, I. & Ohshima, H. (2001). Low Temperature Poly-Si TFTs Using Solid Phase Crystallization of Very Thin Films and an Electron Cyclotron Resonance Chemical Vapor Deposition Gate Insulator, *Japanese Journal of Applied Physics*, Vol. 30. No. 12B, (December 1991), pp. 3724-3728
- Makihara, K.; Nozaki, H.; Asano, T. & Miyasaka, M. (2003). Metal-Induced Lateral Crystallization of Amorphous Silicon under Reduced Nickel Supply, *Solid State Phenomena*, Vol. 93, pp. 207-212
- McCulloch, D. J. & Brotherton, S. D. (1995). Surface Roughness Effects in Laser Crystallized Polycrystalline Silicon, *Applied Physics Letters*, Vol. 66, No. 16, (April 1995), pp. 2060-2062, ISSN 0003-6951
- Menendez, J. & Cardona, M. (1984). Temperature Dependence of the First-Order Raman Scattering by Phonons in Si, Ge, and a-Sn: Anharmonic Effects, *Physical Review B*, Vol. 29, No. 4, (February 1984), pp. 2051-2059
- Mitani, M.; Endo, T.; Taniguchi, Y.; Katou, T.; Shimoto, S.; Ohno, T.; Tsuboi, S.; Okada, T.; Azuma, K.; Kawachi, G. & Matsumura, M. (2008). Ultrahigh-Performance Polycrystalline Silicon Thin-Film Transistors on Excimer-Laser-Processed Pseudo-Single Crystal Films, *Japanese Journal of Applied Physics*, Vol. 47, No. 12, (December 2008), pp. 8707-8713
- Mizuki, T.; Matsuda, J. S.; Nakamura, Y.; Takagi, J. & Yoshida, T. (2004). Large Domains of Continuous Grain Silicon on Glass Substrate for High-Performance TFTs, *IEEE Transactions on Electron Devices*, Vol. 51, No. 2, (February 2004), pp. 204-211, ISSN 0018-9383
- Nakamura, A.; Emoto, F.; Fujii, E.; Yamamoto, A.; Uemoto, Y.; Senda, K. & Kano, G. (1989). Analysis of Solid Phase Crystallization in Amorphized Polycrystalline Si Films on Quartz Substrates, *Journal of Applied Physics*, Vo. 66, No. 9, (November 1989), pp. 4248-4251, ISSN 0021-8979
- Nickel, N. H.; Anderson, G. B. & Johnson R. I. (1997). Grain-Boundary Defects in Laser-Crystallized Polycrystalline Silicon, *Physical Review B*, Vol. 56, No. 19, (November 1997), pp. 12062-12068, ISSN 0163-1829

- Noguchi, T.; Chen, Y.; Miyahira, T.; Mugiraneza, J. D.; Ogino, Y.; Iida, Y.; Sahota, E. & Terao, M. (2010). Advanced Micro-Polycrystalline Silicon Films Formed by Blue-Multi-Laser-Diode Annealing, *Japanese Journal of Applied Physics*, Vol. 49, (March 2010), pp. 03CA10 (3 pages)
- Richter, H.; Wang, Z. P. & Ley, L. (1981). The One Phonon Raman Spectrum in Microcrystalline Silicon, *Solid State Communications*, Vol. 39, pp. 625-629, ISSN 0038-1098
- Roth, J. A.; Olsen, G. L.; Jacobson, D. C. & Poate, J. M. (1990). Kinetics of Solid Phase Epitaxy in Thick Amorphous Si Layers Formed by MeV Ion Implantation, *Applied Physics Letters*, Vol. 57, issue 13, pp. 1340-1342
- Samesima, T.; Usui, S. & Sekiya, M. (1986). XeCl Excimer Laser Annealing Used in the Fabrication of Poly-Si TFT's, *IEEE Electron Device Letters*, Vol. EDL-7, No. 5, (May 1986), pp. 276-278, ISSN 0741-3106
- Sameshima, S. & Usui, S. (1993). Pulsed Laser-Induced Melting Followed by Quenching of Silicon Films, *Journal of Applied Physics*, Vol. 74, No. 11, (December 1993), pp. 6592-6598, ISSN 0021-8979
- Sameshima, T.; Watakabe, H.; Kanno, H.; Sadoh, T. & Miyao, M. (2005). Pulsed Laser Crystallization of Silicon-Germanium Films, *Thin Solid Films*, Vol. 487, pp. 67-71, ISSN 0040-6090
- Sameshima, T. (2009). Laser Crystallization for Large-Area Electronics, *Applied Physics A*, Vol. 96, (April 2009), pp. 137-144
- Secco d' Aragona, F. (1972). Dislocation Etch for (100) Planes in Silicon, *Journal of Electrochemical Societies: Solid State Science and Technology*, Vol. 119, No. 7, (July 1972), pp. 948-951
- Sridharan, M.; Narayandass, Sa. K.; Mangalaraj, D. & Lee, H. C. (2003). Effect of Boron Ion Implantation on the Structural and Optical Properties of Polycrystalline Cd_{0.96}Zn_{0.04}Te Thin Films, *Nuclear Instruments and Methods in Physics Research B*, Vol. 201, pp. 465-474
- Spinella, C.; Lombard, S. & Prioro, F. (1998). Crystal Grain Nucleation in Amorphous Silicon, *Journal of Applied Physics*, Vol. 84, No. 10, (November 1998), pp. 5383-5413, ISSN 0021-8979
- Takahashi, H.; Suezawa, M. & Sumino, K. (1995). Generation and Dissociation of Complexes of Iron and Phosphorus Atoms in Silicon, *Journal of Applied Physics*, Vol. 78, No. 5, (September 1995), pp. 3078-3082, ISSN 0021-8979
- Takayama, T.; Ohtani, H.; Miyanaga, A.; Mitsuki, T.; Ohnuma, H.; Nakajima, S. & Yamazaki, S. (2000). Continuous Grain Silicon Technology and Its Application for Active Matrix Display, *Digest of Technical Papers: AM-LCD 2000*, Tokyo, July 2000, pp. 25-28
- Tanaka, T.; Toko, K.; Sadoh, T. & Miyao, M. (2010). High Quality Single-Crystalline Ge-Rich SiGe on Insulator Structures by Si-Doping Controlled Rapid Melting Growth, *Applied Physics Express*, Vol. 3, (February 2010), pp. 031301 (3 pages)
- Temple, P. A. & Hathaway, C. E. (1973). Multiphonon Raman Spectrum of Silicon, *Physical Review B*, Vol. 7, No. 8, (April 1973), pp. 3685-3697
- Thompson, C. V. (1985). Secondary Grain Growth in Thin Films of Semiconductors: Theoretical Aspects, *Journal of Applied Physics*, Vol. 58, No. 2, (July 1985), pp. 763-772, ISSN 0021-8979

Weizman, M.; Nickel, N.H.; Sieber, I.; Bohne, W.; Rohrich, J.; Strub, E. & Yan, B. (2005). Phase Segregation in Laser Crystallized Polycrystalline SiGe Thin Films, *Thin Solid Films*, Vol. 487, (March 2005), pp. 72-76, ISSN 0040-6090

IntechOpen

IntechOpen

© 2012 The Author(s). Licensee IntechOpen. This is an open access article distributed under the terms of the [Creative Commons Attribution 3.0 License](#), which permits unrestricted use, distribution, and reproduction in any medium, provided the original work is properly cited.

IntechOpen

IntechOpen